Supplementary Material

Orbital Torque in Rare-Earth Transition-Metal Ferrimagnets

Shilei Ding*, Min-Gu Kang, William Legrand, Pietro Gambardella*.

Department of Materials, ETH Zürich, 8093 Zürich, Switzerland

Table of contents

S1. Sample preparation and surface roughness of Gd_yCo_{100-y}/CuO_x

The thin film samples were grown by magnetron sputtering on Si/SiO_2 substrates with a 6-nm-thick Si_3N_4 buffer layer deposited in situ. The preparation of the ferrimagnetic layer Gd_yCo_{1-y} is controlled by tuning the deposition rate of Co and Gd in a confocal direct current (DC) sputtering configuration. The targets are 2 inches in diameter and located 80 mm below the substrates. In principle, the deposition rate is proportional to the applied DC current, which allows us to vary the proportion of Gd from 10% to 35%. The parameters for the deposition of the Gd_yCo_{100-y} layers are reported in Table S1. The values of y represent the nominal relative amount of Gd obtained by calibrating the Gd and Co sources at the target currents reported in Table S1.

Sample	DC current Gd target (mA)	DC current Co target (mA)	Deposition time (s)
$Gd_{20}Co_{80}$	20	75	216
$Gd_{21}Co_{79}$	20	70	224
$Gd_{23}Co_{77}$	20	65	234
$Gd_{24}Co_{76}$	20	60	243
$Gd_{29}Co_{71}$	20	47	269
$Gd_{30}Co_{70}$	20	45	279
$Gd_{32}Co_{68}$	20	40	294
$Gd_{35}Co_{65}$	20	35	310
$Gd_{10}Co_{90}$ (*)	15	108	150
$Gd_{15}Co_{85}$ (*)	20	84	158
$Gd_{24}Co_{76}$ (*)	20	50	220

Table S1. Deposition parameters of the Gd_yCo_{1-y} alloys. The samples were fabricated in two batches: (*) indicates samples from the second batch.

The CuO_x layers were prepared by sputtering of Cu after deposition of Gd_yCo_{100-y} and successive natural oxidation in air for at least two days before lift off and starting the measurements, similar to previous studies of ferromagnetic layers and CuO_x [1-3]. The thickness of CuO_x was chosen to be 6 nm, motivated by the following argument: a CuO_x layer with a thickness smaller than 3 nm would be entirely oxidized in air, leading also to the partial oxidation of the underlying magnetic layer. A CuO_x layer thicker than 10 nm would entail a rather thick region of unoxidized Cu, which would shunt a large part of the current through a region of the sample with a negligible orbital Rashba-Edelstein effect (due to the much smaller O gradient in this region). Thus, too thick Cu will also lead to the reduction of the orbital torque efficiency. The dependence of the orbital torque on the thickness of CuO_x is similar to that reported in Ref. 4.

Figure S1(a) and (b) show atomic force microscopy (AFM) images of $Gd_{20}Co_{80}(10)/CuO_x(6)$ and $Gd_{20}Co_{80}(10)/Pt(5)$, respectively. The root mean square (RMS) roughness of $Gd_{20}Co_{80}(10)/CuO_x(6)$ is 0.27 nm, indicating a relatively flat surface. Some surface grains are visible on the surface, which we attribute to the oxidation of Cu. The RMS roughness of $Gd_{20}Co_{80}(10)/Pt(5)$ is 0.16 nm.

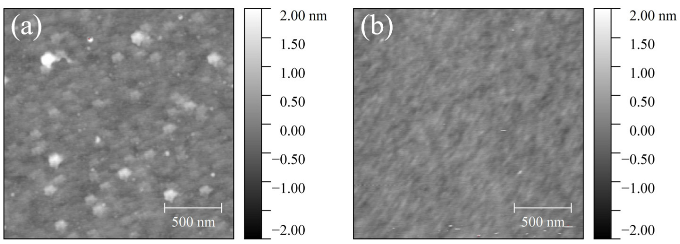

Fig. S1. Surface topography of (a) $Gd_{20}Co_{80}(10)/CuO_x(6)$ and (b) $Gd_{20}Co_{80}(10)/Pt(5)$ measured by AFM.

S2. Magnetization, anomalous Hall resistance, and magnetic anisotropy of Gd_yCo_{100-y} with different capping layers

In order to measure the effective dampinglike field B_{DL}, one needs to know the value of the magnetization M_s, anomalous Hall resistance R_{AHE} and the effective magnetic anisotropy field $B_{\mathrm{dem+ani}}$ (see Eq. S1 in Section S3). Figure S2 shows the magnetization loops measured by a superconducting quantum interference device (SQUID) of representative samples investigated in this work. We observe that changing the top layer does not affect the saturation magnetization of $Gd_{30}Co_{70}$ in a significant way. The values of $M_s t$ required to calculate $\xi_{\mathrm{DL}}^{\mathrm{E}}$ and $\xi_{\mathrm{DL}}^{\mathrm{j}}$ are extracted from a series of such measurements performed for all the samples investigated in this work.

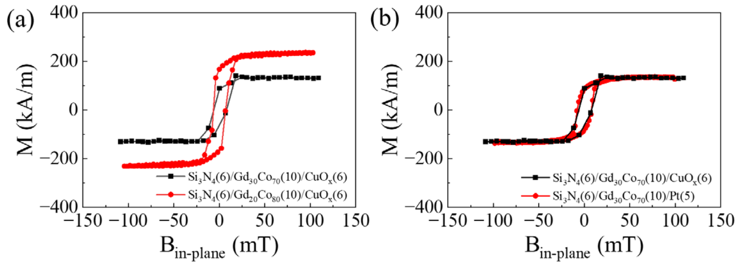

Fig. S2. Magnetic hysteresis loops of (a) $Gd_{30}Co_{70}(10)/CuO_x(6)$ and $Gd_{20}Co_{80}(10)/CuO_x(6)$ and (b) $Gd_{30}Co_{70}(10)/CuO_x(6)$ and $Gd_{30}Co_{70}(10)/Pt(5)$ measured by SQUID at 300 K.

Figure S3 shows the anomalous Hall resistance as a function of the out-of-plane magnetic field of representative samples investigated in this study, namely (a) $Gd_{20}Co_{80}(10)/CuO_x(6)$, (b) $Gd_{30}Co_{70}(10)/CuO_x(6)$, (c) $Gd_{20}Co_{80}(10)/Pt(5)$, and (d) $Gd_{20}Co_{80}(10)/Si_3N_4(6)$. R_{AHE} is obtained by taking the difference of the extrema of the curves shown in Fig. S2 after subtraction of the linear slope due to the ordinary Hall effect. $B_{\mathrm{dem+ani}}$ includes the demagnetizing field and magnetocrystalline anisotropy and is given by the field at which the anomalous Hall resistance saturates as the magnetization points out-of-plane. We obtain $R_{AHE} = 0.1\ \Omega$, and $B_{\mathrm{dem+ani}} = 1.2$ T for $Gd_{20}Co_{80}(10)/CuO_x(6)$ and $R_{AHE} = -0.07\ \Omega$, and $B_{\mathrm{dem+ani}} = 1.5$ T for $Gd_{30}Co_{70}(10)/CuO_x$. We note that the anomalous Hall resistance changes sign as the content of Gd increases and the magnetization crosses the compensation point, as expected [5]. We further find that R_{AHE} increases in $Gd_{20}Co_{80}(10)/Pt(5)$ and $Gd_{20}Co_{80}(10)/Si_3N_4$ (6) relative to the samples with CuO_x due to the reduced current shunting by the nonmagnetic layer.

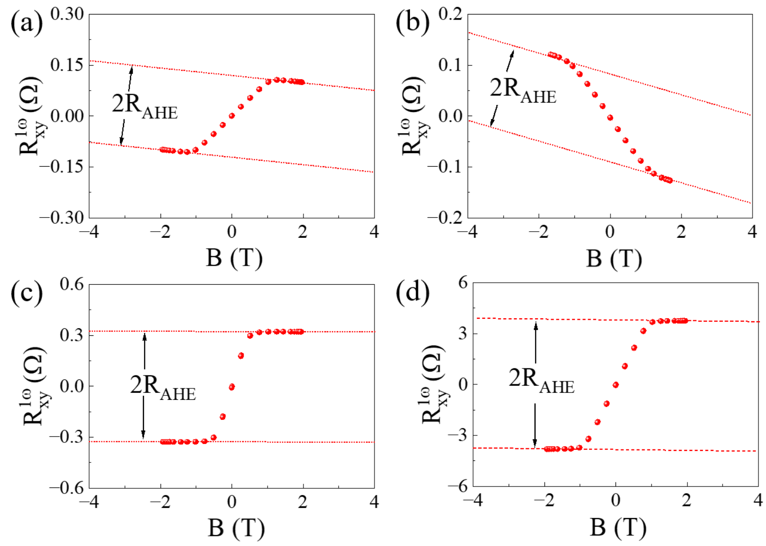

Fig. S3. Anomalous Hall resistance as a function of out-of-plane magnetic field of (a) $Gd_{20}Co_{80}(10)/CuO_x(6)$, (b) $Gd_{30}Co_{70}(10)/CuO_x$ (6), (c) $Gd_{20}Co_{80}(10)/Pt(5)$, and (d) $Gd_{20}Co_{80}(10)/Si_3N_4(6)$. The dotted lines represent the extrema of the anomalous Hall resistance. The linear slope is given by the ordinary Hall effect.

S3. Harmonic Hall resistance measurements of current-induced spin-orbit torques

To measure the orbital torque, we apply an alternate electric current to the sample $I = I_0 \sin \omega t$ of frequency $\omega/2\pi \approx 10$ Hz. The current-induced torque leads to periodic oscillations of the magnetization, which modulates the anomalous Hall effect (AHE) and planar Hall effect (PHE) at the frequency ω, leading to a 2ω component of the Hall voltage $V_{xy}^{2\omega}$ and a second harmonic component of the Hall resistance $R_{xy}^{2\omega} = V_{xy}^{2\omega}/I$. Based on this method, one can derive the effective magnetic fields B_{DL} and B_{FL} corresponding to the dampinglike and fieldlike spin-orbital torques, respectively [6,7]. In order to separate the contribution of B_{DL} and B_{FL} and magnetothermal effects to the second harmonic signal, the measurements of $R_{xy}^{2\omega}$ are performed as a function of the angle φ between the magnetization and current and the external field B_{ext}. For a sample with in-plane magnetization [7]

$$R_{xy}^{2\omega}(\varphi) = \left(\frac{1}{2} R_{AHE} \frac{B_{DL}}{B_{ext}+B_{dem+ani}} + R_{\nabla T}\right) \cos\varphi + R_{PHE} \left(2\cos^3 \varphi - \cos\varphi\right) \frac{B_{FL}+B_{Oe}}{B_{ext}}, \quad \text{(S1)}$$

where R_{AHE} and $B_{dem+ani}$ are obtained as described in Section S2, $R_{\nabla T}$ includes the anomalous Nernst effect and spin Seebeck effect $\sim (\nabla T \times \boldsymbol{M}) \cdot \boldsymbol{y}$ due to the out-of-plane temperature gradient ∇T [7], $\boldsymbol{M}$ is the magnetization, R_{PHE} is the planar Hall resistance and B_{Oe} the Oersted field produced by the current flowing in the nonmagnetic layer, which can be estimated by Ampère's law.

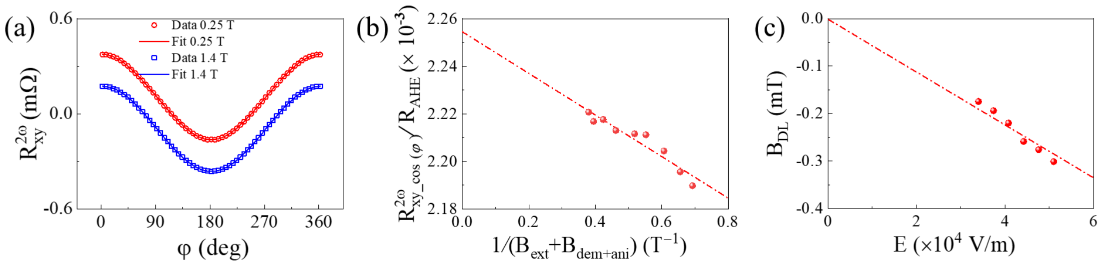

Fig. S4. (a) $R_{xy}^{2\omega}$ of $Gd_{20}Co_{80}(10)/CuO_x(6)$ as a function of the in-plane angle φ measured in an external field of 0.25 T (red circles) and 1.4 T (blue squares) with a current peak value of 10 mA at room temperature. The solid lines are fits to the data according to Eq. (S1). (b) $R_{xy\_\cos\varphi}^{2\omega}/R_{AHE}$ vs $(B_{ext} + B_{dem+ani})^{-1}$. The dashed line is a linear fit. The negative slope of the fits shows that the torque has a negative sign relative to Co/CuO_x and Gd_yCo_{100-y}/Pt. The effective field B_{DL} is -0.17 ± 0.01 mT for a current of 10 mA, which corresponds to an applied electric field $E = I\frac{R_{xx}^{1\omega}}{L} = 3.4\times 10^4$ V/m, where $R_{xx}^{1\omega}$ is the first harmonic longitudinal resistance and L is the length of the Hall bar. (c) B_{DL} as a function of the electric field. The dashed line is a linear fit, which gives $\xi_{DL}^{E} = \frac{2e}{\hbar} M_s t_{GdCo} B_{DL}/E$ = $-3.9 \pm 0.2 \times 10^4\ \Omega^{-1}\text{m}^{-1}$.

Figure S4(a) presents the angular dependence of $R_{xy}^{2\omega}(\varphi)$ of $Gd_{20}Co_{80}(10)/CuO_x(6)$ at room temperature for two different values of the applied field, B_{ext} = 0.25 and 1.4 T, and a current peak value I_0 =10 mA. Fitting the curves with Eq. (1) allows us to separate the first term proportional to $\cos\varphi$, $R_{xy\_\cos\varphi}^{2\omega} = \left(\frac{1}{2} R_{AHE} \frac{B_{DL}}{B_{ext}+B_{dem+ani}} + R_{\nabla T}\right)$, from the second proportional to $(2\cos^3\varphi - \cos\varphi)$. Then, a linear fit of $R_{xy\_\cos\varphi}^{2\omega}/R_{AHE}$ vs $(B_{ext} + B_{dem+ani})^{-1}$ gives B_{DL} as two times the slope of the fit and $R_{\nabla T}$ as the intercept for $(B_{ext} + B_{dem+ani})^{-1} \to 0$, as shown in Fig. S4(b). By repeating this procedure for different values of the applied electric field or current, one finally obtains B_{DL} as a function of E or I_0 [Fig. S4(c)], which provides the torque efficiency per unit applied electric field, $\xi_{DL}^{E} =$

$\frac{2e}{\hbar} M_\mathrm{s} t_\mathrm{GdCo} B_\mathrm{DL}/E$, and current, $\xi^\mathrm{j}_\mathrm{DL} = \frac{2e}{\hbar} M_\mathrm{s} t_\mathrm{GdCo} B_\mathrm{DL}/j = \xi^\mathrm{E}_\mathrm{DL}\rho$. Here $M_\mathrm{s} t_\mathrm{GdCo}$ is the areal magnetic moment, which is obtained from the total magnetic moment measured using a SQUID magnetometer and dividing it by the sample area.

From the in-plane angular scan, we obtain $R_\mathrm{PHE} = 0.0015\ \Omega$. Fitting the curves in Fig. S4(a) with Eq.(1) allows us to separate the second term proportional to $(2\cos^3\varphi - \cos\varphi)$, $R^{2\omega}_{\mathrm{xy\_}(2\cos^3\varphi-\cos\varphi)} = R_\mathrm{PHE}\,(2\cos^3\varphi - \cos\varphi)\frac{B_\mathrm{FL}+B_\mathrm{Oe}}{B_\mathrm{ext}}$. We thus obtain the $(B_\mathrm{FL} + B_\mathrm{Oe})/I_0$ = 0.1 mT/mA. Assuming $B_\mathrm{Oe} \approx \frac{I}{2w} = 0.063$ mT/mA, we can further separate the field-like torque from the torque due to the Oersted field. However, the precise value of B_Oe depends on the distribution of the current in the bilayer. We thus focus on the damping-like torque in this study.

S4. Damping-like torque in $Gd_{30}Co_{70}$ with different top layers

In this section, we present the harmonic Hall voltage measurements of a $Gd_{30}Co_{70}$(10) layer coupled to CuO_x(6), Pt(5), and Si_3N_4(6) layers. As the composition of the ferrimagnetic layer changes from $Gd_{20}Co_{80}$ to $Gd_{30}Co_{70}$, the magnetization changes from Co-dominant to Gd-dominant at room temperature, which implies that the magnetic field dependence of the AHE, Nernst effect, and spin Seebeck effect reverse their sign [8]. Thus, the in-plane angular φ dependence of $R^{2\omega}_\mathrm{xy}(\varphi)$ is reversed in $Gd_{30}Co_{70}$ compared to $Gd_{20}Co_{80}$, as shown in Fig. S5(a,b) compared to Fig. S4(a). By fitting the curves in Fig. S5 as described in Section S3, we extract B_DL for $Gd_{30}Co_{70}$(10)/CuO_x(6) and $Gd_{30}Co_{70}$(10)/Pt(5). B_DL is negative in $Gd_{30}Co_{70}$(10)/CuO_x(6), i.e., it has the same sign and the same effect on the net magnetization as in $Gd_{20}Co_{80}$(10)/CuO_x(6). Instead, B_DL is positive in $Gd_{30}Co_{70}$(10)/Pt(5) as expected for spin injection from Pt. The opposite sign of B_DL in these two samples is evident from the opposite slope of the curves shown in Fig. S5(c-f).

Figure S6 presents the harmonic Hall resistance measurements of $Gd_{30}Co_{70}$(10)/Si_3N_4(6), a second control sample without either CuO_x or Pt, in addition to $Gd_{20}Co_{80}$(10)/Si_3N_4(6) presented in the main text. As seen by the flat dependence of $R^{2\omega}_\mathrm{xy\_cos\varphi}$ vs $(B_\mathrm{ext} + B_\mathrm{dem+ani})^{-1}$ and B_DL vs E, we can exclude the presence of a significant self-torque ($\xi^\mathrm{E}_\mathrm{DL} = (0.014 \pm 0.005) \times 10^4\ \Omega^{-1}\mathrm{m}^{-1}$) produced by current injection in Gd_yCo_{100-y} also in this sample.

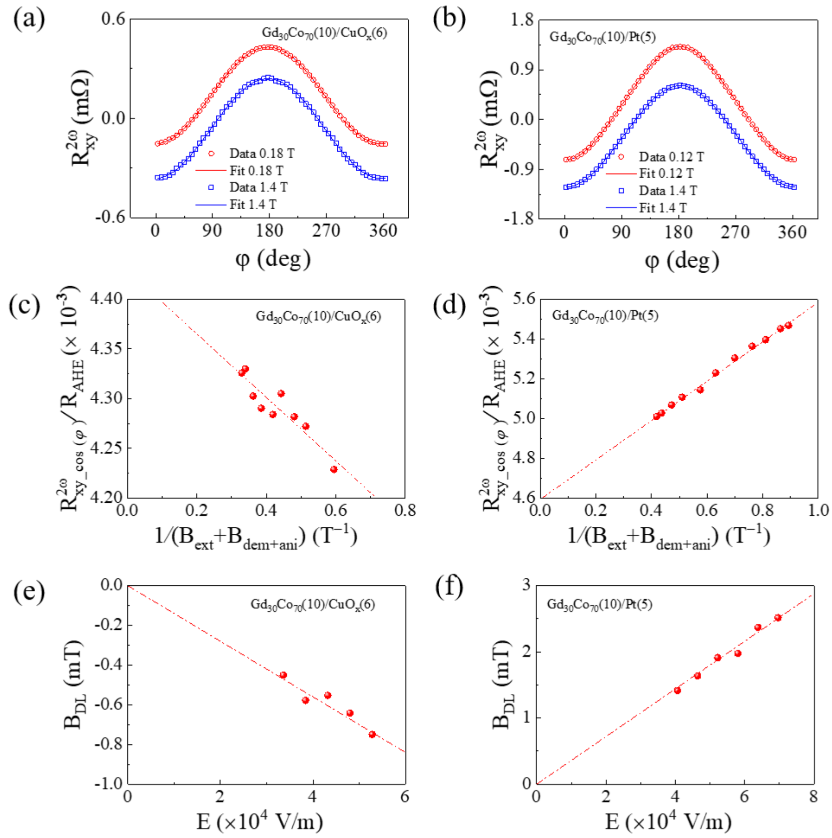

Fig. S5. $R_{xy}^{2\omega}$ of (a) Gd30Co70(10)/CuOx(6) and (b) Gd30Co70(10)/Pt(5) as a function of the in-plane angle φ measured in an external field of 0.18 T (red circles) and 1.4 T (blue squares) with a current peak value of 10 mA at room temperature. The solid lines are fits to the data according to Eq. (S1). (c,d) $R_{\mathrm{xy\_cos}\varphi}^{2\omega}/R_{\mathrm{AHE}}$ vs $(B_{\mathrm{ext}}+B_{\mathrm{dem+ani}})^{-1}$ for the two samples. (e,f) B_{DL} as a function of the electric field. The dashed lines are the linear fits used to calculate $\xi_{\mathrm{DL}}^{\mathrm{E}}$ for the two samples.

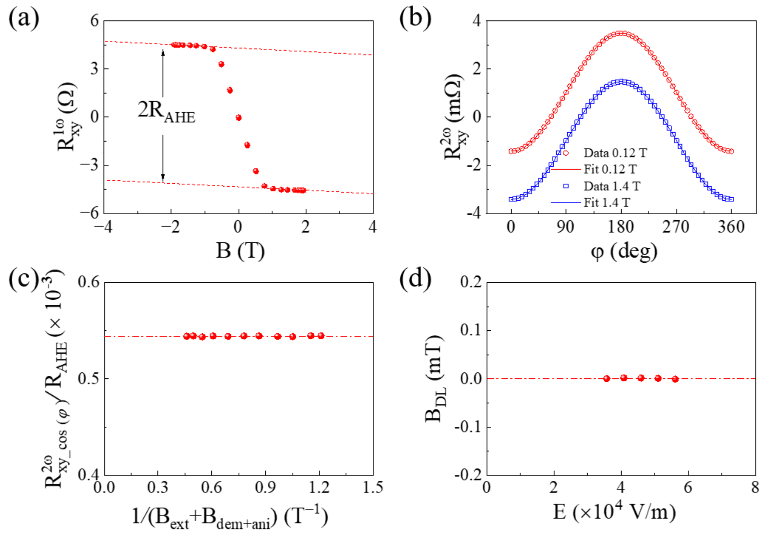

Fig. S6. (a) Anomalous Hall resistance as a function of the out-of-plane magnetic field of Gd30Co70(10)/Si3N4(6). (b) $R_{xy}^{2\omega}$ as a function of the in-plane angle φ measured in an external field of 0.12 T (red circles) and 1.4 T (blue squares) with a current peak value of 10 mA at room temperature. The solid lines are fits to the data according to Eq. (S1). (c) $R_{\mathrm{xy\_cos}(\varphi)}^{2\omega}/R_{\mathrm{AHE}}$ $(B_{\mathrm{ext}}+B_{\mathrm{dem+ani}})^{-1}$. (d) B_{DL} as a function of the electric field. The dashed lines are linear fits to the data.

S5. Longitudinal resistance and effective spin Hall angle $\xi_{\mathrm{DL}}^{\mathrm{j}}$ in $\mathrm{Gd_yCo_{100-y}/CuO_x}$

Figure S7 shows the longitudinal resistance R_{xx} of $\mathrm{Gd_yCo_{100-y}(10)/CuO_x(6)}$ as a function of Gd concentration. We notice an increase of R_{xx} by about 50% as y increases from 0.20 to 0.35. This increase of resistance does not affect the estimation of $\xi_{\mathrm{DL}}^{\mathrm{E}}$, which is normalized by the applied electric field $E = \rho j$, where ρ is the resistivity of the $\mathrm{Gd_yCo_{100-y}/CuO_x}$ bilayer and j the applied current density.

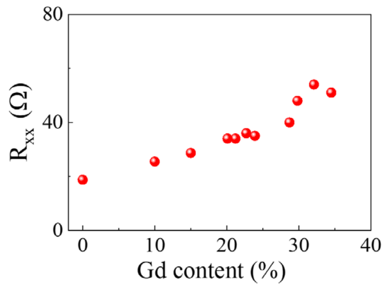

Fig. S7. Longitudinal resistance of $\mathrm{Gd_yCo_{100-y}(10)/CuO_x(6)}$ as a function of Gd content.

The effective spin-orbital Hall angle $\xi_{\mathrm{DL}}^{\mathrm{j}} = \xi_{\mathrm{DL}}^{\mathrm{E}}\rho$, on the other hand, is affected by the resistivity of the layers. Figure S8 shows $\xi_{\mathrm{DL}}^{\mathrm{j}}$ as a function of temperature corresponding to the data reported in Fig. 4 of the main text. Because the current distribution in the $\mathrm{CuO_x}$ layers is not precisely known, we consider here the average resistivity $\rho = R_{xx}w/l$, where $w = l = 10\ \mu\mathrm{m}$ and average current density $j = I_0/w$. We find that $\xi_{\mathrm{DL}}^{\mathrm{j}}$ follows the similar trend as $\xi_{\mathrm{DL}}^{\mathrm{E}}$ as a function of composition and temperature, which is expected given the relatively small resistance variations compared to the amplitude of the orbital torque.

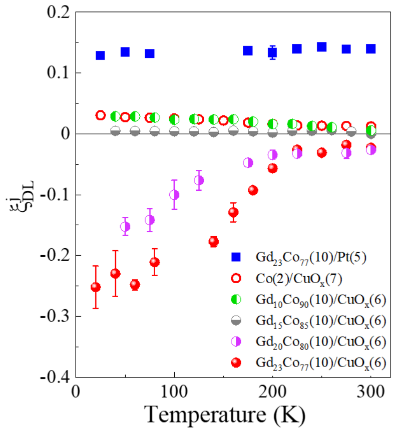

Fig. S8. Temperature dependence of the effective spin-orbital Hall angle $\xi_{\mathrm{DL}}^{\mathrm{j}}$ in $\mathrm{Co(2)/CuO_x(7)}$, $\mathrm{Gd_{23}Co_{77}(10)/Pt(5)}$ and different $\mathrm{Gd_yCo_{100-y}(10)/CuO_x(6)}$ samples.

S6. Torque and magnetization measurements as a function of temperature in samples with different amounts of Gd

Figure S9 shows the temperature dependence of M_s, torque efficiency ξ_{DL}^{E}, and longitudinal resistance of different $Gd_yCo_{100-y}(10)/CuO_x(6)$ samples. All samples were measured at room temperature within about 4 weeks from deposition. The temperature-dependent measurements of $Co(2)/CuO_x(7)$, $Gd_{10}Co_{90}(10)/CuO_x(6)$, $Gd_{15}Co_{85}(10)/CuO_x(6)$, $Gd_{23}Co_{77}(10)/CuO_x(6)$, and an additional control sample of $Gd_{24}Co_{76}(10)/CuO_x(6)$ deposited in a second batch were also taken within 4 weeks from deposition. The temperature-dependent measurements of $Gd_{20}Co_{80}(10)/CuO_x(6)$ and $Gd_{24}Co_{76}(10)/CuO_x(6)$ were carried out 11 months after sample fabrication. The resistance of these aged samples is larger due to the increased oxidation of the CuOx layer. The comparison between measurements carried out on the "fresh" and aged samples of $Gd_{24}Co_{76}(10)/CuO_x(6)$ shows that both M_s and ξ_{DL}^{E} are not strongly affected by aging.

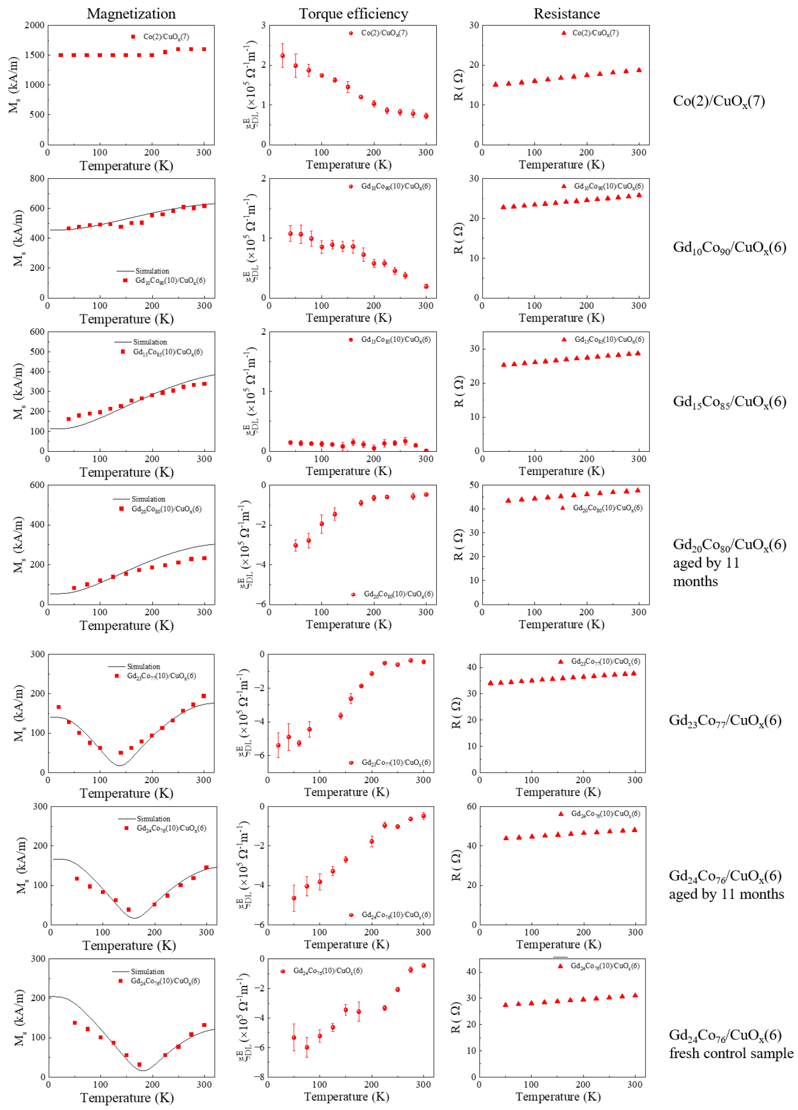

Fig. S9. Temperature dependence of the saturation magnetization, torque efficiency, and longitudinal resistance of $Co(2)/CuO_x(7)$ and $Gd_yCo_{100-y}(10)/CuO_x(6)$. The solid curves in the first column are simulations of M_s based on the mean-field model described in Section 7.

S7. Mean field model of the temperature dependence of the magnetization in Gd_yCo_{100-y}/CuO_x

The temperature dependence of M_s and sublattice magnetizations M_{Gd} and M_{Co} can be modeled by using a mean-field approximation based on the so-called environment model [9-13]. We take the magnetic moments per atom of bulk Gd and Co at zero temperature to be $m_{\mathrm{Gd}}^{\mathrm{at}}(0) = 7\,\mu_{\mathrm{B}}$ and $m_{\mathrm{Co}}^{\mathrm{at}}(0) = 1.71\,\mu_{\mathrm{B}}$ and consider the reduction of the atomic moment of Co in the alloy due to the decreasing number of transition-metal nearest neighbors. The average atomic magnetic moment of Co as a function of Gd content y is given by

$$m_{\mathrm{Co}}(0) = m_{\mathrm{Co}}^{\mathrm{at}}(0)\ \sum_{k=j}^{L} \frac{L!}{(L-k)!k!}\left(\frac{100-y}{100}\right)^{k}\left(\frac{y}{100}\right)^{L-k}, \tag{S2}$$

where $L = 12$ is the maximum coordination number and $j = 7$ for Co [9,10]. The effective magnetic fields acting on the Gd and Co sublattices are

$$h_{\mathrm{Gd}} = h + \gamma_{\mathrm{Co\_Gd}} N_{\mathrm{Co}} m_{\mathrm{Co}}(T) + \gamma_{\mathrm{Gd\_Gd}} N_{\mathrm{Gd}} m_{\mathrm{Gd}}(T), \tag{S3}$$

and

$$h_{\mathrm{Co}} = h + \gamma_{\mathrm{Co_{Gd}}} N_{\mathrm{Gd}} m_{\mathrm{Gd}}(T) + \gamma_{\mathrm{Co_{Co}}} N_{\mathrm{Co}} m_{\mathrm{Co}}(T), \tag{S4}$$

where h is the applied external field. Here $\gamma_{\mathrm{Co\_Co}} = \lambda_{\mathrm{Co\_Co}} Z_{\mathrm{Co}}/(N_{\mathrm{Co}} g_{\mathrm{Co}}^2 \mu_{\mathrm{B}}^2)$ is the exchange interaction per Co atom with $\lambda_{\mathrm{Co\_Co}}$ the exchange coupling per Co-Co pair, Z_{Co} the average number of nearest neighbor Co atoms around one Co atom, and $g_{\mathrm{Co}} = 2.2$. Similarly, we have $\gamma_{\mathrm{Gd\_Gd}} = \lambda_{\mathrm{Gd\_Gd}} Z_{\mathrm{Gd}}/(N_{\mathrm{Gd}} g_{\mathrm{Gd}}^2 \mu_{\mathrm{B}}^2)$, $\gamma_{\mathrm{Co\_Gd}} = \lambda_{\mathrm{Co\_Gd}} Z_{\mathrm{Co\_Gd}}/(N_{\mathrm{Gd}} g_{\mathrm{Co}} g_{\mathrm{Gd}} \mu_{\mathrm{B}}^2)$ and $g_{\mathrm{Gd}} = 2$. $N_{\mathrm{Co}} = \frac{100-y}{100}N$ and $N_{\mathrm{Gd}} = \frac{y}{100}N$ are the number of magnetic atoms of Co and Gd and N is the total number of the magnetic atoms. The maximum number of nearest neighbors is 12 in the amorphous samples [10], and we have $Z_{\mathrm{Co}} = 12 \times \frac{100-y}{100}$, $Z_{\mathrm{Gd}} = 12 \times \frac{y}{100}$ and $Z_{\mathrm{Co\_Gd}} = 12 \times \frac{y}{100}$. According to Eqs. S3-S4, the mean-field magnetic moments of Gd and Co are given by:

$$m_{\mathrm{Gd}}(T) = m_{\mathrm{Gd}}(0)\mathcal{B}\left[\frac{m_{\mathrm{Gd}}(0) h_{\mathrm{Gd}}}{kT}\right], \tag{S5}$$

$$m_{\mathrm{Co}}(T) = m_{\mathrm{Co}}(0)\mathcal{B}\left[\frac{m_{\mathrm{Co}}(0) h_{\mathrm{Co}}}{kT}\right], \tag{S6}$$

where $\mathcal{B}$ is the Brillouin function, k is the Boltzmann constant and T is the temperature.

The volumetric saturation magnetization of each sublattice is then calculated as:

$$M_{\mathrm{Gd}}(T) = \frac{y\, m_{\mathrm{Gd}}(T)}{(100-y)v_{\mathrm{Co}} + y v_{\mathrm{Gd}}}, \tag{S7}$$

$$M_{\mathrm{Co}}(T) = \frac{(100-y) m_{\mathrm{Co}}(T)}{(100-y)v_{\mathrm{Co}} + y v_{\mathrm{Gd}}}, \tag{S8}$$

where $v_{\mathrm{Gd}} = 3.3 \times 10^{-29} m^3$ and $v_{\mathrm{Co}} = 1.1 \times 10^{-29} m^3$ are the atomic volumes of Gd and Co.

In general, the exchange parameters $\lambda_{\mathrm{Co\_Co}} > \lambda_{\mathrm{Co\_Gd}} > \lambda_{\mathrm{Gd\_Gd}}$ are a function of the composition of the alloy [9,11]. Similar to Refs. [9,11], we take $\lambda_{\mathrm{Co\_Co}}$ decreasing monotonically from $1.8 \times 10^{-22}\,J$ (10% Gd) to $1.2 \times 10^{-22}\,J$

(24% Gd), which reflects the decrease in exchange strength between the Co atoms due to increased bonding with Gd, we vary λ_{Co_Gd} between $2.5 \times 10^{-23}\,J$ and $2.8 \times 10^{-23}\,J$ and keep $\lambda_{Gd\_Gd} = 2.2 \times 10^{-23}\,J$ as a constant. Further, we allow for deviations from the nominal stoichiometry of Gd of up to $\Delta y = 1$ in order to account for unintentional differences between the nominal and actual composition of the samples. With these parameters, we can simulate M_s and the separate temperature dependence of M_{Gd} and M_{Co}, as shown for $Gd_{23}Co_{77}(10)/CuO_x(6)$ in Fig. S10. We stress that, given the assumptions of the mean field model and the number of unknown parameters, these simulations are only indicative of the actual behavior of $M_{Gd}(T)$ and $M_{Co}(T)$.

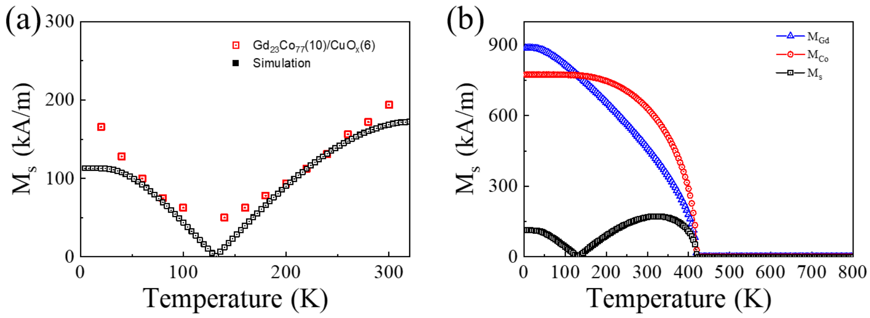

Fig. S10. (a) Temperature dependence of the saturation magnetization of $Gd_{23}Co_{77}(10)/CuO_x(6)$ measured by SQUID. The black squares are the simulated M_s using the mean field approximation for a single composition of $y = 22$. (b) Simulated magnetizations of the Co and Gd sublattices from the mean-field approximation with the exchange interaction parameters $\lambda_{Co\_Co} = 1.2 \times 10^{-21}\,J$, $\lambda_{Gd\_Gd} = 2.2 \times 10^{-23}\,J$ and $\lambda_{Co\_Gd} = 2.5 \times 10^{-23}\,J$.

Better fits of the saturation magnetization $M_s = |M_{Co}(T) - M_{Gd}(T)|$ can further be obtained by considering a Gaussian distribution of the stoichiometry around a mean value y_0 with standard deviation $\sigma = 0.5$. The inhomogeneous stoichiometry accounts for the nonzero experimental value of M_s around the compensation temperature observed in Fig. S9. At each temperature we simulate $M_s(T, y_0) = \sum f(y_i) M_s(T, y_i) / \sum f(y_i)$, where $f(y) = \frac{1}{\sigma\sqrt{2\pi}} e^{-\frac{(y-y_0)^2}{2\sigma^2}}$ and y_i varies evenly from $y_0 - 1$ to $y_0 + 1$ in steps of $\Delta y = 0.2$. The solid lines in Fig. S9 have been obtained in this way.

Experimentally, the magnetic compensation temperature T_M is determined from the saturation magnetization obtained from magnetic hysteresis loops measured by SQUID at different temperatures on unpatterned samples. Measurements of the anomalous Hall resistance after lift-off show that T_M is similar to the value obtained from the magnetic hysteresis loop measurement on the full film, see, e.g., Fig. 3(a) and 4(a) in the main text.

S8. Correlation between torque efficiency and magnetization in Gd_yCo_{100-y}/CuO_x

Figure S11 shows the relative change in temperature of the following quantities:

(a) orbital torque efficiency $\Delta\xi_{\mathrm{DL}}^{\mathrm{E}}/\xi_{\mathrm{DL}}^{\mathrm{E}}(300\ \mathrm{K}) = \frac{[\xi_{\mathrm{DL}}^{\mathrm{E}}(50\ \mathrm{K}) - \xi_{\mathrm{DL}}^{\mathrm{E}}(300\ \mathrm{K})]}{\xi_{\mathrm{DL}}^{\mathrm{E}}(300\ \mathrm{K})}$,

(b) simulated sublattice saturation magnetizations $\Delta M_{\mathrm{s},i}/M_{\mathrm{s},i}(300\ \mathrm{K}) = \frac{[M_{\mathrm{s},i}(50\ \mathrm{K}) - M_{\mathrm{s},i}(300\ \mathrm{K})]}{M_{\mathrm{s},i}(300\ \mathrm{K})}$ with i = Gd, Co,

(c) saturation magnetization $\Delta M_{\mathrm{s}}/M_{\mathrm{s}}(300\ \mathrm{K}) = \frac{[M_{\mathrm{s}}(50\ \mathrm{K}) - M_{\mathrm{s}}(300\ \mathrm{K})]}{M_{\mathrm{s}}(300\ \mathrm{K})}$,

(d) longitudinal resistance $\Delta R/R(300\ \mathrm{K}) = \frac{[R(50\ \mathrm{K}) - R(300\ \mathrm{K})]}{R(300\ \mathrm{K})}$.

The orbital torque efficiency $\xi_{\mathrm{DL}}^{\mathrm{E}}$ increases monotonically with Gd concentration upon lowering temperature, similar to the sublattice magnetizations M_{Gd} and M_{Co}. No clear correlation is found between the change of $\xi_{\mathrm{DL}}^{\mathrm{E}}$ and the saturation magnetization M_{s} and longitudinal resistance R.

We note also that we do not expect a strong influence of the magnetic field on the orbital-to-spin conversion ratio. That is because the magnetizations M_{s}, M_{Co}, and M_{Gd} are strongly temperature and composition-dependent, but saturate at moderate fields (see Fig. S2 and S3). In agreement with these considerations, we do not observe significant nonlinear effects in the torque measurements performed as a function of field, i.e., in the curves of $R_{\mathrm{xy\_cos}(\varphi)}^{2\omega}/R_{\mathrm{AHE}}$ vs $(B_{\mathrm{ext}} + B_{\mathrm{dem+ani}})^{-1}$.

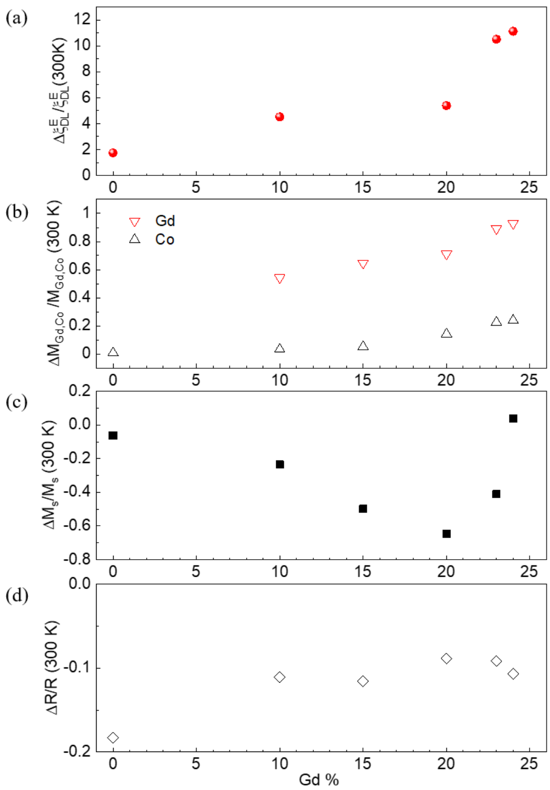

Fig. S11. Relative change with temperature of (a) orbital torque efficiency, (b) simulated sublattice saturation magnetizations, (c) saturation magnetization, and (d) resistance as a function of Gd concentration. The data points in (b) are simulated using the model described in Section S7. The simulated values of $\Delta M_{\mathrm{s},i}/M_{\mathrm{s},i}$ have been calculated for a single stoichiometry, they change by less than 5% when using a weighted Gaussian distribution of the stoichiometry (see Sect. 7 for details).

S9. Temperature dependence of B_{DL} in $Gd_{23}Co_{77}$(10)/CuO_x(6) and $Gd_{24}Co_{76}$(10)/CuO_x(6)

Figure S12 shows the temperature dependence of B_{DL} normalized by current in $Gd_{23}Co_{77}$(10)/CuO_x(6) and $Gd_{24}Co_{76}$(10)/CuO_x(6). We note that B_{DL} diverges at the magnetic compensation temperature, as expected when M_s tends to zero [5].

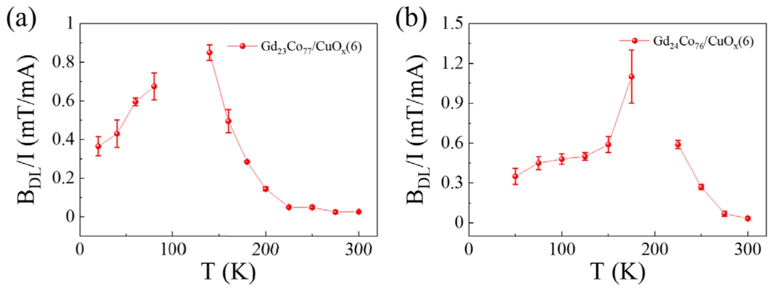

Fig. S12. Temperature dependence of B_{DL}/I in (a) $Gd_{23}Co_{77}$(10)/CuO_x(6) and (b) $Gd_{24}Co_{76}$(10)/CuO_x(6).

S10. Discussion of the sign of the orbital torque

The data presented in Fig. 4 of the main text and Fig. S12 show that the orbital torque does not change sign across the magnetic compensation point of GdCo. Thus, the orbital torque behaves in the same way as the spin torque measured in Pt/GdCo [this work and Refs. 14,15]. In all of these cases the effective damping-like field B_{DL} and $\xi_{\mathrm{DL}}^{\mathrm{E}}$ do not change sign across either the compensation temperature T_M or composition y_M.

This behaviour can be understood by considering that the damping-like torque reflects the absorption of angular momentum $\boldsymbol{\sigma}$ from an external source, which does not change sign with temperature. The damping-like torque is defined as $\boldsymbol{T}_{\mathrm{DL}} \sim \boldsymbol{M} \times \boldsymbol{M} \times \boldsymbol{\sigma} \sim \boldsymbol{\sigma}$ and does not depend on the sign of $\boldsymbol{M}$. On the other hand, the damping-like effective field is defined as $\boldsymbol{B}_{\mathrm{DL}} \sim \boldsymbol{M} \times \boldsymbol{T}_{\mathrm{DL}} \sim \boldsymbol{M} \times \boldsymbol{\sigma}$, which depends on the sign of $\boldsymbol{M}$. However, by this definition, $\boldsymbol{M}$ is the net magnetization, which does not change sign across T_M for a given orientation of the applied magnetic field. Thus, also B_{DL} does not change sign.

This reasoning does not change as M_{Gd} inverts at T_M. The sign of the spin-orbit coupling in the 5d orbitals of Gd remains negative, meaning that an incoming orbital current with transverse polarization along, say, $\hat{\boldsymbol{\zeta}}$ is converted by Gd in a spin current polarized along $-\hat{\boldsymbol{\zeta}}$. Because the incoming orbital current has a constant sign, also the converted spin current has a constant sign below and above T_M. Therefore, for an external angular momentum source, be it of spin or orbital character, we do not expect a change of sign of B_{DL} and $\xi_{\mathrm{DL}}^{\mathrm{E}}$.

Supplementary References

1. H. An, Y. Kageyama, Y. Kanno, N. Enishi, and K. Ando, Spin–Torque Generator Engineered by Natural Oxidation of Cu, *Nat. Commun*. **7**, 13069 (2016).
2. Y. Kageyama, Y. Tazaki, H. An, T. Harumoto, T. Gao, J. Shi, and K. Ando, Spin-Orbit Torque Manipulated by Fine-Tuning of Oxygen-Induced Orbital Hybridization, *Sci. Adv*. **5**, eaax4278 (2019).
3. S. Ding et al., Harnessing Orbital-to-Spin Conversion of Interfacial Orbital Currents for Efficient Spin-Orbit Torques, *Phys. Rev. Lett.* **125**, 177201 (2020).
4. J. Kim et al., Oxide Layer Dependent Orbital Torque Efficiency in Ferromagnet/Cu/Oxide Heterostructures, *Phys. Rev. Mater.* **7**, L111401 (2023).
5. J. Finley and L. Liu, Spin-Orbit-Torque Efficiency in Compensated Ferrimagnetic Cobalt-Terbium Alloys, *Phys. Rev. Appl*. **6**, 54001 (2016).
6. K. Garello, I. M. Miron, C. O. Avci, F. Freimuth, Y. Mokrousov, S. Blügel, S. Auffret, O. Boulle, G. Gaudin, and P. Gambardella, Symmetry and Magnitude of Spin-Orbit Torques in Ferromagnetic Heterostructures, *Nat. Nanotechnol.* **8**, 587 (2013).
7. C. O. Avci, K. Garello, M. Gabureac, A. Ghosh, A. Fuhrer, S. F. Alvarado, and P. Gambardella, Interplay of Spin-Orbit Torque and Thermoelectric Effects in Ferromagnet/Normal-Metal Bilayers, *Phys. Rev. B* **90**, 224427 (2014).
8. S. Geprägs et al., Origin of the Spin Seebeck Effect in Compensated Ferrimagnets, *Nat. Commun*. **7**, 10452 (2016).
9. P. Hansen, C. Clausen, G. Much, M. Rosenkranz, and K. Witter, Magnetic and Magneto-optical Properties of Rare-earth Transition-metal Alloys Containing Gd, Tb, Fe, Co, *J. Appl. Phys*. **66**, 756 (1989).
10. D. H. Suzuki, M. Valvidares, P. Gargiani, M. Huang, A. E. Kossak, and G. S. D. Beach, Thickness and Composition Effects on Atomic Moments and Magnetic Compensation Point in Rare-Earth Transition-Metal Thin Films, *Phys. Rev. B* **107**, 134430 (2023).
11. A. Gangulee and R. J. Kobliska, Mean Field Analysis of the Magnetic Properties of Amorphous Transition-metal–Rare-earth Alloys, *J. Appl. Phys*. **49**, 4896 (1978).
12. P. J. von Ranke, N. A. de Oliveira, B. P. Alho, E. J. R. Plaza, V. S. R. de Sousa, L. Caron, and M. S. Reis, Understanding the Inverse Magnetocaloric Effect in Antiferro- and Ferrimagnetic Arrangements, *J. Phys. Condens. Matter* **21**, 56004 (2009).
13. D. H. Suzuki, B. H. Lee, and G. S. D. Beach, Compositional Dependence of Spintronic Properties in Pt/GdCo Films, *Appl. Phys. Lett*. **123**, 122401 (2023).
14. R. Mishra, J. Yu, X. Qiu, M. Motapothula, T. Venkatesan, and H. Yang, Anomalous Current-Induced Spin Torques in Ferrimagnets near Compensation, *Phys. Rev. Lett.* **118**, 167201 (2017).
15. L. Caretta et al., Fast Current-Driven Domain Walls and Small Skyrmions in a Compensated Ferrimagnet, *Nat. Nanotechnol*. **13**, 1154 (2018).